Research Article

Xi Luo, Yuqin Dong, Dongying Wang, Yujie Duan, Ke Lei, Linjiao Mao, Ying Li, Qiang Zhao*, and Yan Sun*

Facile synthesis of g-C₃N₄ nanosheets for effective degradation of organic pollutants *via* ball milling

https://doi.org/10.1515/rams-2023-0123 received June 06, 2023; accepted September 15, 2023

Abstract: Graphitic carbon nitride (g-C₃N₄) has attracted extensive research interest in pollutants remediation. However, the photocatalytic activity of g-C₃N₄ was significantly limited by its small specific surface area. In this work, a green, highenergy ball milling method was used to fabricate g-C₃N₄ nanosheets. The structure, morphology, and optical properties of the prepared g-C₃N₄ nanosheets were characterized. The effect of ball milling parameters on the photocatalytic performance evaluated by Rhodamine B (RhB) and tetracycline (TC) was investigated systemically. Among the tested samples, the g-C₃N₄ sample milled with a 4 mL isopropanol solution at a rotation speed of 420 rpm, ball-to-powder weight ratio of 10:1, and milling time of 24 h exhibited the highest RhB degradation efficiency of 91.4% and TC degradation efficiency of 70.2%. The enhanced photocatalytic activity after ball milling was ascribed to the increase in specific surface area and efficient separation of electronhole pairs. The trapping experiment indicated that holes and superoxide radicals were the main active species in the degradation reaction. Moreover, the photocatalytic degradation mechanism of organic pollutants on g-C₃N₄ nanosheets was also discussed in detail.

Keywords: g-C₃N₄ nanosheets, ball milling, photocatalysis

Xi Luo, Yuqin Dong, Dongying Wang, Yujie Duan, Ke Lei, Linjiao Mao, Ying Li: School of Mechanical Engineering, Chengdu University, Chengdu, 610106, China

1 Introduction

Owing to technological advancements and rapid industrialization, environmental pollution problems, especially water pollution, have increased dramatically in many countries. Organic pollutants, in particular, are harmful to human health and ecosystems due to their stable, carcinogenic, soluble, and nondegradable properties [1]. Semiconductor photocatalysis is a promising and popular technology for decomposing and mineralizing organic pollutants using renewable solar energy. In recent decades, graphitic carbon nitride (g-C₃N₄) has been extensively studied in the field of photocatalysis due to its moderate bandgap energy, high thermal stability, low cost, and good redox properties [2-4]. However, the application of g-C₃N₄ obtained from the traditional thermal polymerization method is greatly restricted by the insufficient active sites, small specific surface area, low quantum efficiency, and high recombination rate of the photogenerated electron-hole pairs [5]. To date, various modification strategies have been reported to enhance the catalytic properties of g-C₃N₄ through morphology control, surface area increase, elemental doping, and heterostructure construction [6-9]. Therefore, the structure of a photocatalyst is an important factor affecting its catalytic activity.

It is widely known that g-C₃N₄ nanosheets exhibit a high specific surface area, wide bandgap, and prolonged lifetime of photogenerated carriers and thus show great promise for wastewater purification [10–12]. Currently, thermal, chemical, and mechanical exfoliation are regarded as effective strategies to obtain g-C₃N₄ nanosheets. For example, Li *et al.* [13] reported that g-C₃N₄ nanosheets prepared by thermal oxidation could accelerate the separation of the photogenerated electron–hole pairs. Wu *et al.* [14] prepared g-C₃N₄ nanosheets with a large specific surface area by calcining bulk g-C₃N₄ at 600°C repeatedly seven times, and the obtained g-C₃N₄ nanosheets showed nitric oxide removal efficiency of 35.8%. Zhang *et al.* [15] successfully synthesized ultrathin g-C₃N₄ nanosheets *via* ultrasonic

^{*} Corresponding author: Qiang Zhao, School of Chemical Engineering, Sichuan University, Chengdu, 610065, China, e-mail: scuzq@scu.edu.cn

^{*} Corresponding author: Yan Sun, School of Mechanical Engineering, Chengdu University, Chengdu, 610106, China, e-mail: sunyan@cdu.edu.cn

exfoliation in different liquids. Although several methods have been developed to fabricate g-C₃N₄ nanosheets, the low yield and complicated processing limit their applications. Ball milling with high speed can produce shear and compressive normal force, which has a broad application prospect in semiconductor modification. Ma et al. [16] prepared g-C₃N₄ nanosheets via a facile ball milling method at various ball milling speeds, which demonstrated that ball milling can provide more active sites and improve photocatalytic degradation. Zhu et al. [17] synthesized g-C₃N₄/SnO₂ heterojunction using ball milling and revealed that ball milling could change the surface morphology and structure of the catalysts, thus facilitating charge transfer and prolonging the carrier lifetimes. Thereby, ball milling technology has been considered a simple and effective method to enhance the photocatalytic performance of g-C₃N₄. Up to now, there have been few reports on the systematic study of ball milling parameters for g-C₃N₄.

In this study, a green ball milling strategy was used to fabricate $g\text{-}C_3N_4$ nanosheets in different solvents. The effects of the rotation speed, ball-to-powder weight ratio, milling time, and solvent content on the photocatalytic performance were systematically investigated. The photocatalytic activity was evaluated by the degradation of Rhodamine B (RhB) and tetracycline (TC) under simulated solar illumination. In addition, the possible photocatalytic degradation mechanism was explored by determining the active species. This study provides opportunities for the design and application of $g\text{-}C_3N_4$ photocatalysts in the field of environmental remediation.

2 Experimental

2.1 Preparation of $g-C_3N_4$ nanosheets

Bulk g- C_3N_4 (denoted as CN) was synthesized by thermal polymerization. Typically, 5 g of melamine was placed in an alumina crucible and heated at 550°C for 4 h in a muffle furnace at a rate of 5°C·min⁻¹. After calcination, the prepared yellow powder was washed with deionized water and dried.

As shown in Scheme 1, the $g-C_3N_4$ nanosheets were prepared by ball milling CN powder with different solvents in a planetary ball mill (QM-3SP04). The CN powder (1.0 g) was loaded into the ball mill tank with agate balls of different mass and a specified amount of solvent (2, 4, and 6 mL) and milled for the specified time. Ball milling was performed at different ball-to-powder weight ratios (5:1, 10:1, 15:1, and 20:1), rotation speeds (240, 300, 360, and 420 rpm), and milling

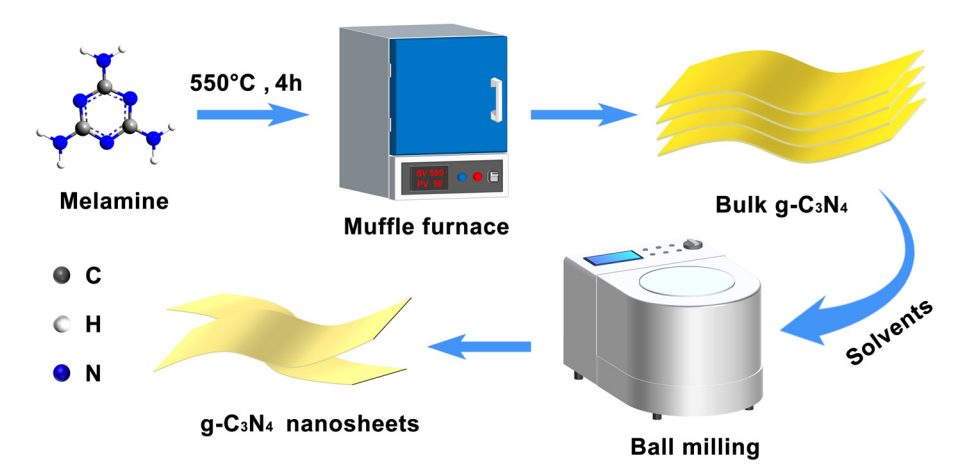
times (12, 24, 36, and 48 h). The obtained suspension was collected by centrifugation, washed successively with deionized water and ethanol, and dried at 70°C for 2 h. The samples milled with isopropanol (IPA), ethanol, and deionized water are denoted as ICN, ECN, and DCN, respectively. For comparison, the sample milled without the addition of solvent is denoted as MCN. When determining the effects of milling factors (except for milling time) on photocatalytic performance, samples milled for 24 h were used.

2.2 Characterization

The crystal phases of the samples were determined using X-ray diffraction (XRD) on a DX-2700B diffractometer at 40 kV and 30.0 mA using Cu Kα radiation. Scanning electron microscopy (SEM; ZEISS Gemini-300) was used to characterize the morphology of the catalysts. The microstructures of the samples were examined using field-emission transmission electron microscopy (TEM; Talos-F200S). The surface chemical states and valence band (VB) of catalysts were determined by X-ray photoelectron spectroscopy using an ESCALAB Xi+ spectrometer (Thermo Fisher). The surface area was determined using the Brunauer-Emmett-Teller (BET) method on an adsorption apparatus (V-Sorb 2800P). UV-Vis diffuse reflection spectroscopy was performed using a Persee TU-1901 spectrophotometer with BaSO₄ as the reference. Photoluminescence (PL) spectra were measured using an Edinburgh Instruments FLS1000 fluorescence spectrometer with an excitation wavelength of 350 nm. Electron spin resonance (ESR) spectroscopy was performed on Bruker EMXplus using 5,5-dimethyl-1-pyrroline N-oxide (DMPO) as a radical capture reagent.

2.3 Photoelectrochemical measurements

The photocurrent measurements were carried out via an electrochemical workstation (VersaSTAT3) in a standard three-electrode system. A 0.5 M Na₂SO₄ aqueous solution was used as the electrolyte. A Pt net and saturated calomel electrode (SCE) were used as the counter electrode and reference electrode, respectively. The working electrode was prepared as follows: 40 mg of catalyst was mixed in 1 mL of ethylene glycol and 20 μ L of Nafion 117, then ultrasonically dispersed for 30 min to obtain slurry. A 40 μ L of the slurry was uniformly coated on fluorine-dope tin oxide (FTO) glasses with a fixed area of 1 cm \times 1 cm and dried under 70°C. The transient photocurrent response was performed under a 500 W Xe lamp (AM 1.5, 100 mW cm⁻²)



Scheme 1: Schematic of the preparation of g-C₃N₄ nanosheets.

irradiation with 30 s on-off cycle at a voltage of 0.4 V (vs SCE). The electrochemical impedance spectroscopy (EIS) measurements were carried out at the frequency range of 10 kHz to 0.01 Hz. Mott-Schottky curves were measured at a frequency of 1,000 Hz.

2.4 Photocatalytic activity

The photocatalytic activity of the obtained catalysts was evaluated using RhB and TC decomposition under simulated sunlight irradiation (AM 1.5). A 500 W Xe lamp (CEL-S500) with a light intensity of 100 mW cm⁻² was used as the light source. For the test, 0.1 g of catalyst was dispersed in 100 mL of RhB (10 mg·L⁻¹) aqueous solution. For TC degradation, 0.04 g of catalyst was added to the 100 mL TC solution (20 mg·L⁻¹). Prior to illumination, the mixed suspension was magnetically stirred in the dark for 30 min to achieve an adsorption-desorption equilibrium. During irradiation, 5 mL of the suspension was collected and centrifuged at intervals of 10 min for subsequent photocatalytic activity analysis using a UV-Vis spectrophotometer.

2.5 Active species trapping test

For the purpose of exploring the main active species during the photocatalytic reaction, the trapping experiment was carried out using various scavengers. Triethanolamine (TEOA) 15 mM, tert-butyl alcohol (TBA, 10 mM), and 1,4-benzoquinone (BQ, 1 mM) were used to capture holes (h⁺), hydroxyl radicals (OH), and superoxide radicals (O₂⁻) during the photocatalytic process, respectively.

3 Results and discussion

3.1 Structure and chemical composition analysis

Figure 1 shows the XRD patterns of CN and ICN milled with 4 mL IPA for 12 and 24 h. CN and ICN show similar XRD peaks at 13.4° and 27.4°, corresponding to the in-plane repeated units of tri-s-triazine (100) and the interplanar stacking peak of aromatic systems (002) (ICPDS 87-1526). respectively [18]. It is worth noting that the peak intensity of ICN is lower and the peaks are broader than those of CN, indicating that the interlayer structure of g-C₃N₄ was partially destroyed during ball milling. During the ball milling process, the impact force produced between grinding balls can break the weak interplanar van der Waals bonds through combined shearing and stretching [19]. With the increase in ball milling time, the crystallization of g-C₃N₄ in the (002) plane can be destroyed so that the sample can be effectively exfoliated [20].

The chemical states of bulk CN and ICN were further analyzed by X-ray photoelectron spectroscopy (XPS). The survey scans the XPS spectra (Figure 2a) of the two samples to prove the existence of C and N elements. For the C 1s spectrum of the CN sample in Figure 2b, the peaks at 284.8, 286.0, and 288.4 eV are assigned to the carbon atom in the C-C bonds, sp³-bonded carbon (C-N), and sp² N-C=N bonds, respectively [21]. In Figure 2c, the N 1s spectrum of CN can be deconvoluted into three peaks located at 398.6, 400.1, and 401.1 eV, which can be attributed to the sp² hybridized nitrogen (C-N=C group), the bridge nitrogen (N-(C)₃ group), and the N-H bond, respectively [22,23]. Compared with CN, no obvious variation in the binding energy of C 1s and N 1s can be observed after the ball milling process, which is consistent with the previous research [24].

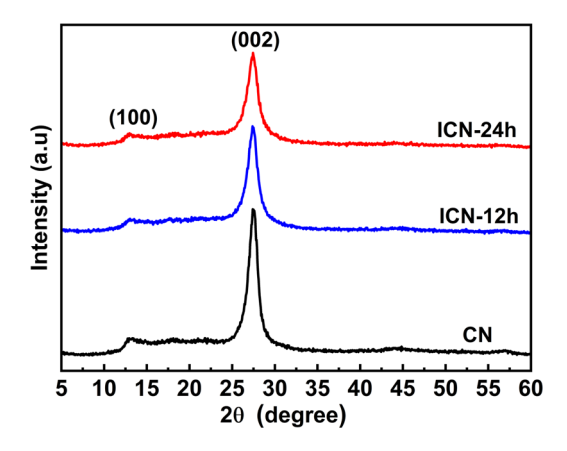


Figure 1: XRD patterns of CN and ICN with different milling times.

3.2 Morphology

The morphology of the prepared CN, ICN, and MCN samples is shown in Figure 3. Clearly, CN (Figure 3a) exhibits an irregular layered structure with a tight stack, which is the typical structure of g-C₃N₄ synthesized using the polymerization method. After ball milling in 4 mL IPA with 420 rpm for 24 h, ICN (Figure 3b) displays a laminar structure with a small particle size, which demonstrates that the g-C₃N₄ nanosheets are successfully exfoliated from the CN. However, as shown in Figure 3(c), when the ball milling of CN was treated without solvent, the particle size of the MCN sample became larger because of severe agglomeration instead of the layer structure. Thus, dispersion of g-C₃N₄ powder in the liquid environment during ball milling could prevent the agglomeration of particles [16].

TEM technique was applied to further investigate the fine structure of CN and ICN. As observed in Figure 4, ICN displays an ultrathin 2D sheet-like structure. Compared with bulk CN, the thickness of ICN is much smaller, which confirms that CN can be exfoliated into g- C_3N_4 nanosheets via the ball milling method.

3.3 Effect of ball milling parameters on photocatalytic performance

3.3.1 Effect of ball milling time

The effect of ball milling time on the photocatalytic degradation of RhB is shown in Figure 5. For the ICN photocatalyst (Figure 5a), the absorbance of RhB decreases with the increase in irradiation time, indicating the gradual degradation of the organic pollutant. Figure 5b compares the degradation efficiency of various g-C₃N₄ samples under the same prepared conditions except for the ball milling time. Without ball milling treatment, the degradation only reaches 30.9%. With the extension of ball milling time to 24 h, the degradation efficiency of ICN significantly increases to 91.4% after 40 min of illumination. However, with a further increase in ball milling time to 36 h, a slight decrease in removal efficiency is observed. Furthermore, the reaction rate constant for photocatalytic degradation can be calculated using the following equation [25]:

$$ln(C_0/C) = kt,$$
(1)

where C_0 is the initial concentration of the pollutant, C is the residual concentration of the pollutant degraded by the photocatalyst, and k is the kinetic constant. As shown in Figure 5c, the RhB degradation reaction of all samples follows pseudo-first-order kinetics model. The reaction rate constant of ICN-24 h reaches a maximum value of 0.05405 min⁻¹, which is 5.0 times higher than that of CN (0.00901 min⁻¹).

The photocatalytic performance of the prepared samples was also evaluated by degradation of TC under light irradiation. As expected in Figure 6a, ICN samples exhibit higher photocatalytic activity than CN, and the highest degradation efficiency of 70.2% is achieved when the ball milling time is 24 h. Similarly, the degradation rate of TC over all photocatalysts also follows the first-order kinetics (Figure 6b), and ICN-24 h shows the highest degradation

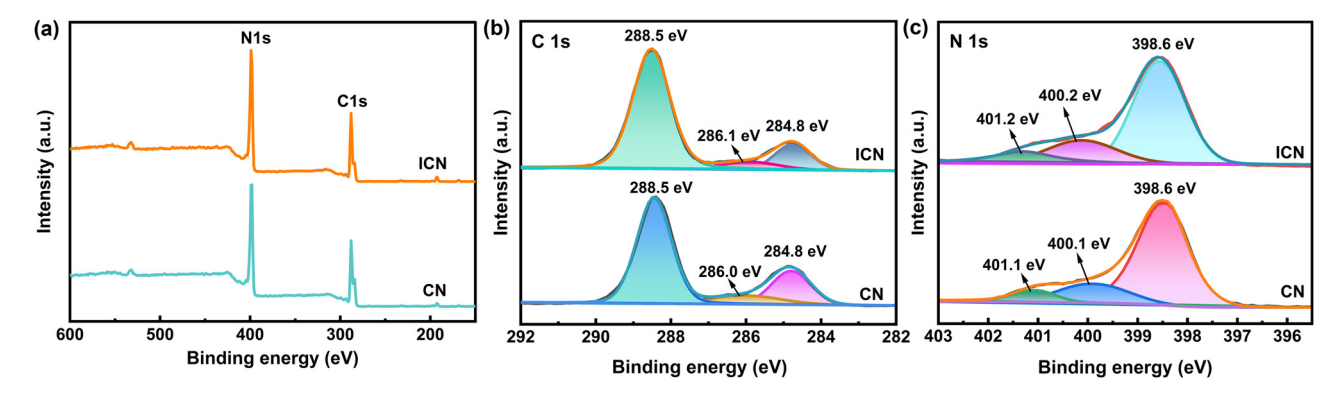


Figure 2: XPS spectra of CN and ICN samples: (a) survey spectrum; (b) C 1s and (c) N 1s.

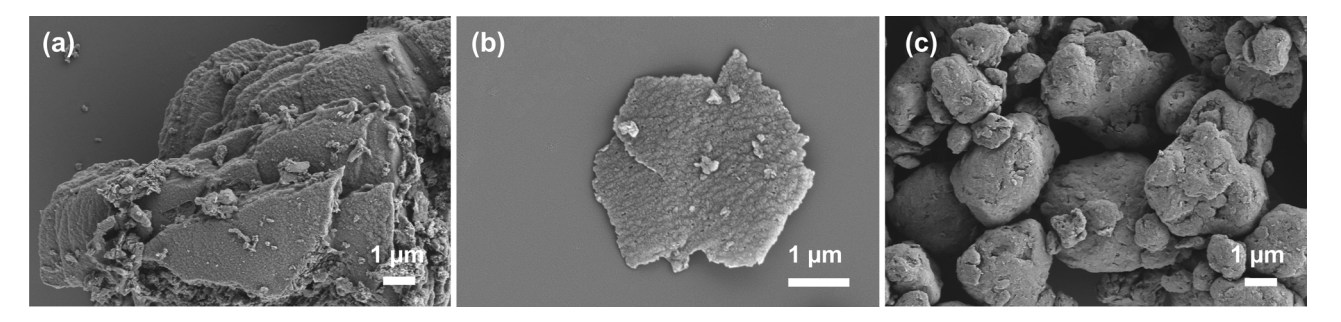


Figure 3: SEM images of the prepared samples: (a) CN, (b) ICN, and (c) MCN.

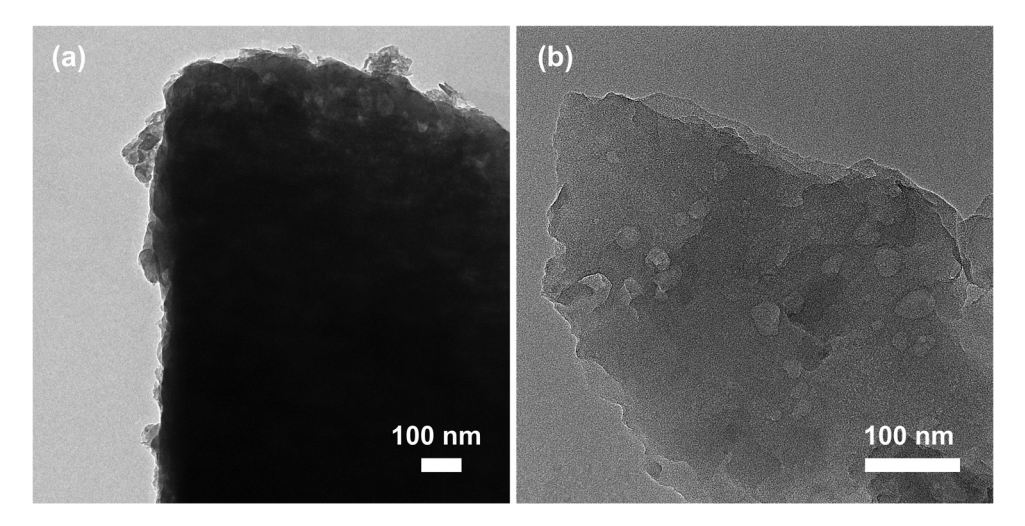


Figure 4: TEM images of (a) CN and (b) ICN.

rate constant of 0.01987 min⁻¹, which is 2.4 times higher than that of CN (0.00585 min⁻¹). This result is consistent with the degradation of RhB, which can be explained by the specific surface area of catalysts. As shown in Figure 6c, the specific surface areas of the samples milled for 0, 12, 24, and 36 h are 12.9, 27.4, 35.1, and 34.5 m²·g⁻¹, respectively. As is well known, a higher specific surface area can generate more photoinduced electrons and provide more contact areas for organic pollutants, thus improving the photocatalytic activity. Ball milling is an effective way to decrease the particle size and increase the specific surface area of samples. However, when the ball milling time exceeds 24 h, small ICN particles tend to agglomerate due to the high surface energy, leading to a decrease in the specific surface area [26]. To improve milling efficiency and save energy, 24 h is selected as the optimal ball milling time.

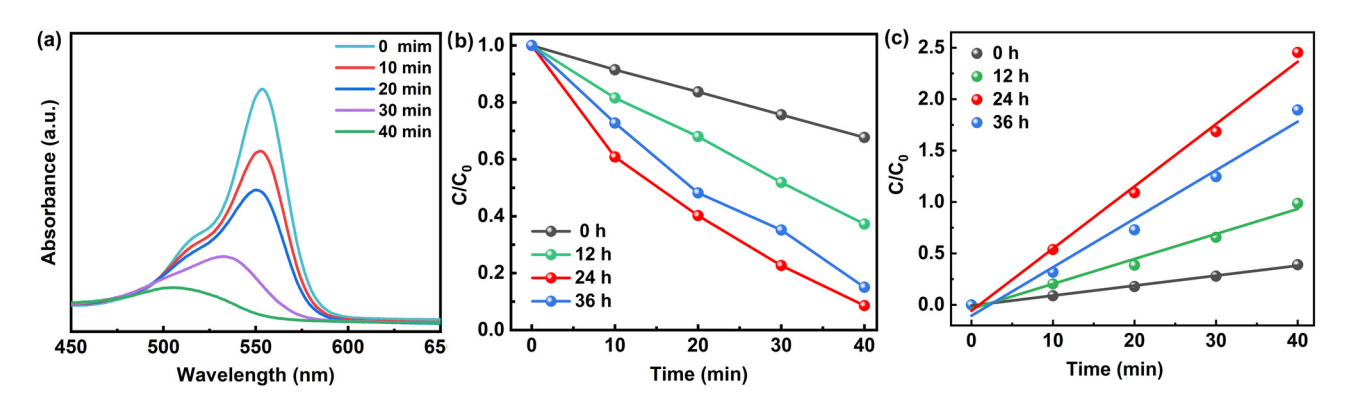


Figure 5: (a) UV-Vis absorption spectra of RhB over ICN milled for 24 h; (b) comparison of photocatalytic activity; and (c) first-order kinetics curves.

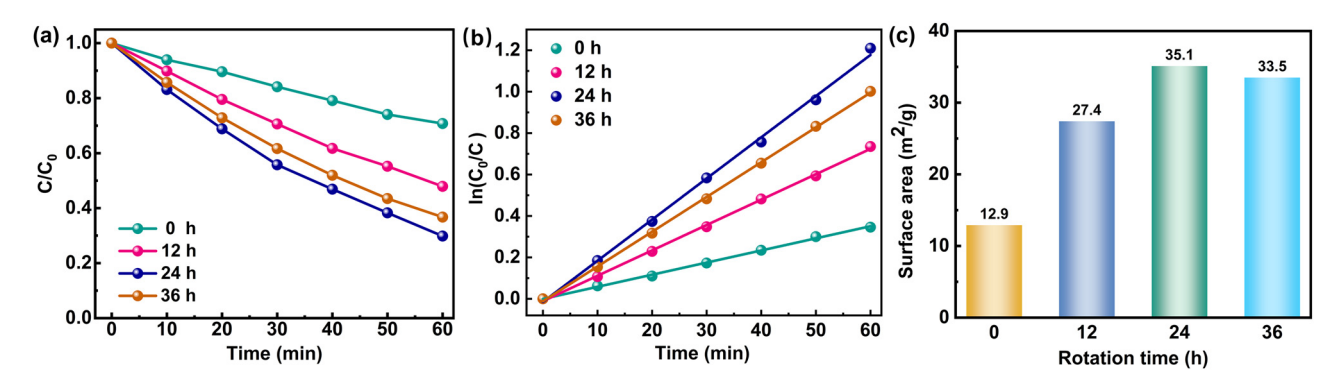


Figure 6: (a) Photocatalytic degradation of TC, (b) first-order kinetics curves, and (c) specific surface area of samples milled for 0, 12, 24, and 36 h.

3.3.2 Effect of rotation speed

Figure 7 shows the photocatalytic activity of the samples obtained at different rotation speeds. As shown in Figure 7a, the ICN sample milled at 420 rpm exhibits the highest RhB degradation efficiency of 91.4% within 40 min. Moreover, it can also be found that the prepared samples exhibit lower photocatalytic activity in TC degradation (Figure 7b). After 60 min of irradiation, only 70.2% of TC can be degraded. Notably, both of the removal efficiencies of RhB and TC increase with increasing rotation speed from 240 to 420 rpm. Similarly, the specific surface area of the samples also increases with the ball milling speed (Figure 7c). As a result of higher rotation speed, the kinetic energy of grinding balls increases [27], and the specific surface area becomes larger, which is beneficial to the degradation of pollutants.

3.3.3 Effect of various solvents

The effect of solvent during the ball milling process on the photocatalytic activity is shown in Figure 8. The RhB degradation efficiency of CN, DCN, ECN, and ICN is 30.9, 40.6,

74.6, and 91.4%, respectively. The same degradation trend occurs in the decomposition of TC (Figure 8b). It can be clearly seen that the introduction of a solvent during ball milling plays an important role in the photocatalytic reaction. The specific surface areas of DCN, ECN, and ICN (Figure 8c) are 24.1, 33.2, and 35.1 m²·g⁻¹, respectively, and are all higher than CN. It has been found that the polarity of the solvents and surface tension are strongly correlated with the exfoliation performance [28]. Among all the solvents with different polarities and surface tension, IPA seems to be a more promising grinding aid.

3.3.4 Effect of IPA volume

Figure 9a shows the degradation performance of the ball-milled samples with different amounts of IPA. For MCN sample, only 5.7% of RhB is decomposed within 40 min, while the degradation efficiency of ICN milled in 4 mL IPA reaches 91.4%. However, with a further increase in the IPA volume, the photocatalytic activity of the sample slightly decreases. A similar trend of TC degradation is found in Figure 9b. Under light irradiation for 60 min,

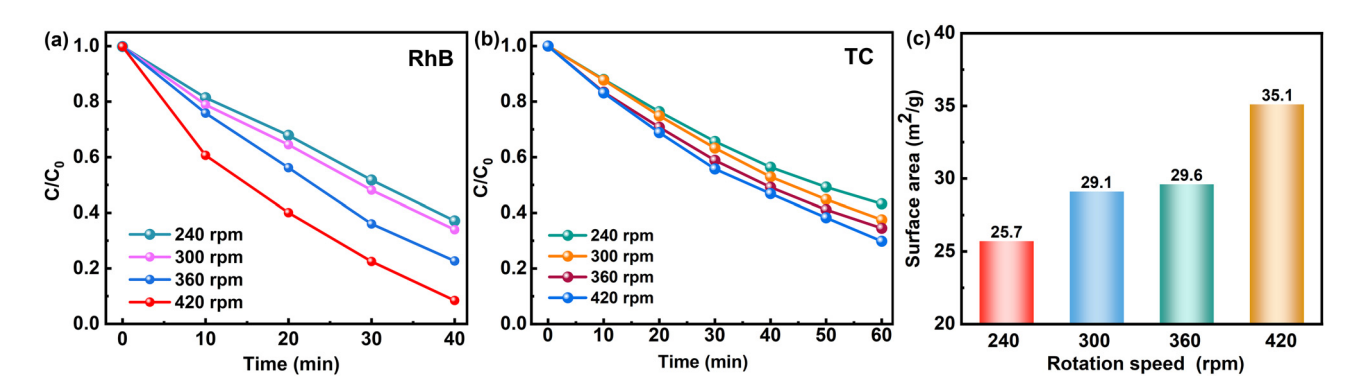


Figure 7: Photocatalytic degradation efficiency of (a) RhB and (b) TC; (c) specific surface area of samples obtained at different rotation speeds with 4 mL IPA for 24 h.

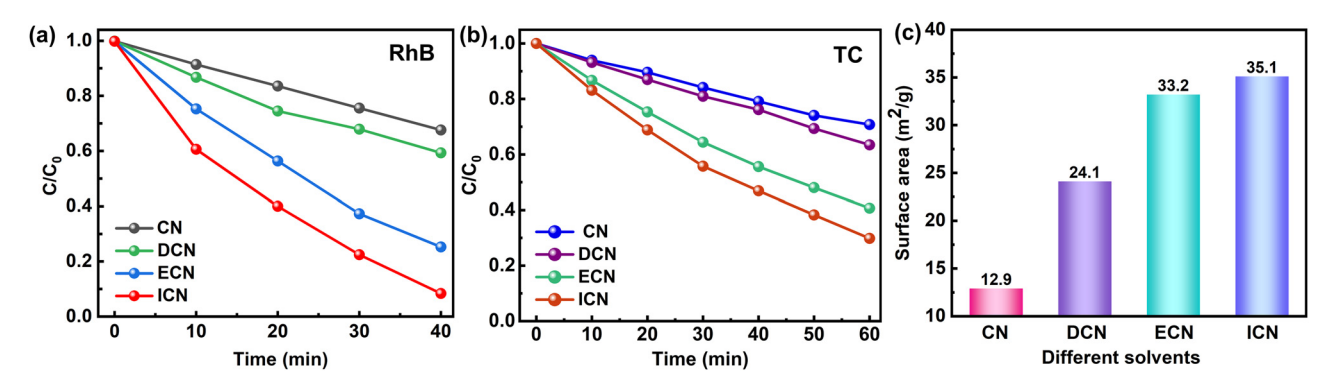


Figure 8: Photocatalytic degradation of (a) RhB and (b) TC; (c) specific surface areas of catalysts milled with various solvents for 24 h at 420 rpm.

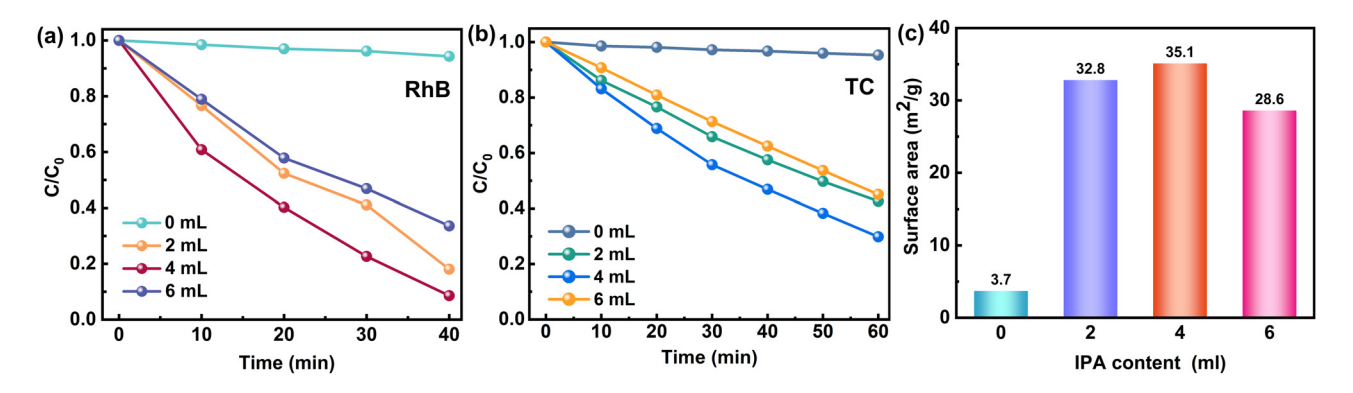


Figure 9: Photocatalytic performance of (a) RhB and (b) TC; (c) specific surface area of the samples milled with different volumes of IPA.

when the volume of IPA increases from 0 to 6 mL, the removal efficiency increases first and then decreases, which is attributed to the difference in the specific surface area of catalysts (Figure 9c). Hence, an appropriate amount of solvent is conducive to restraining particle agglomeration and promoting crack propagation in large particles [29]. However, an excess of solvent in ball milling could prevent CN powder from adsorbing onto the surface of agate balls [30], resulting in a reduction in reaction activity.

3.3.5 Effect of ball-to-powder weight ratio

The ball-to-powder weight ratio is an important variable in ball milling. At the weight ratio of 5:1, the RhB degradation efficiency of ICN is 66.2% (Figure 10a). At the ball-to-powder weight ratio of 10:1, the sample exhibits the highest degradation capacity, with an RhB removal efficiency of 91.4%. As the ball-to-powder weight ratio increases from 15:1 to 20:1, the degradation efficiency decreases from 74.5 to

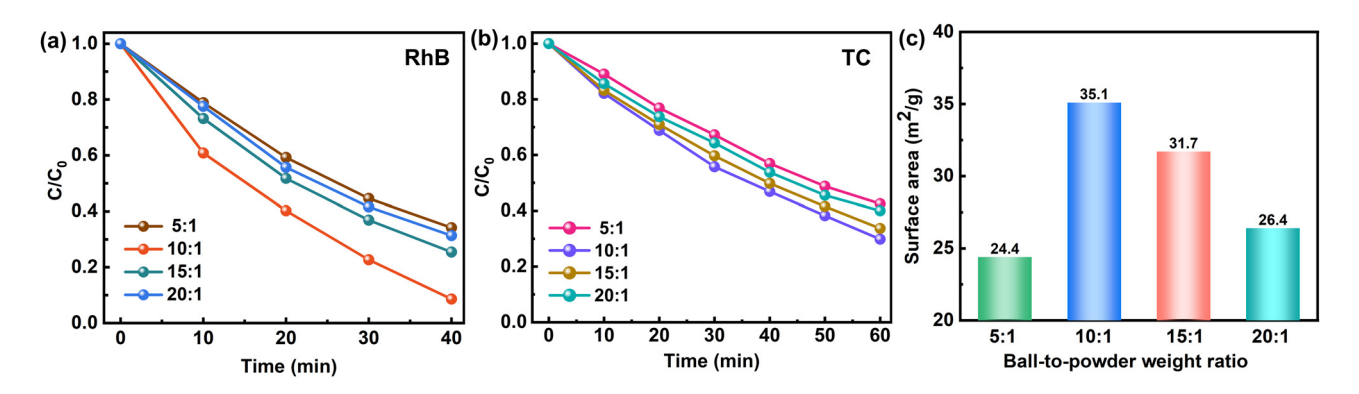


Figure 10: Comparison of the degradation efficiency of (a) RhB and (b) TC; (c) specific surface area of ICN milled at different ball-to-powder weight ratios (24 h, 420 rpm, and 4 mL IPA).

68.7%. For TC degradation, degradation curves (Figure 10b) show the same trend. The specific surface areas of the samples are measured and shown in Figure 10c. The specific surface areas of the catalysts obtained at the ball-to-powder weight ratios of 5:1, 10:1, 15:1, and 20:1 are 24.4, 35.1, 31.7, and 26.4 m²·g⁻¹, respectively. The higher the ball-to-powder weight ratio, the more the contact chance between the powder and the grinding balls, thus increasing the number of powder collisions per unit time [31]. As the ball-to-powder weight ratio exceeds the optimum value, the high filling rate restricts the movement of the agate balls and milled material, causing a decline in the specific surface area [30].

3.4 Optical properties

UV-Vis diffuse reflectance spectra were obtained to examine the optical absorption properties of the CN and ICN catalysts. In Figure 11a, the maximum absorption edge of CN is observed at 463 nm, while the optical absorption edge of ICN shows a distinct blue shift to

445 nm. The bandgap energy of the samples can be calculated using the following formula:

$$\alpha h \nu = A(h \nu - E_g)^2, \tag{2}$$

where α , h, v, A, and $E_{\rm g}$ are the absorption coefficient, Planck's constant, light frequency, proportionality constant, and bandgap energy, respectively [32]. The bandgap values of CN and ICN are 2.57 and 2.78 eV (Figure 11b), respectively. The increased bandgap energy and blue shift can be attributed to the well-known quantum confinement effect caused by ball milling [33].

To further determine the band structure of the catalyst, XPS VB was used to measure the VB positions of ICN. As shown in Figure 11c, the VB value of the sample can be estimated using the following formula [34]:

$$E_{\text{NHE}} = \phi + E_{\text{VL}} - 4.44,$$
 (3)

where $E_{\rm NHE}$, $E_{\rm VL}$, and ϕ are the potential of the normal hydrogen electrode (NHE), the potential of the vacuum level, and the electron work function of the instrument (4.6 eV), respectively. The measured VB and conduction band (CB) potentials of ICN are +2.43 and -0.35 eV, respectively.

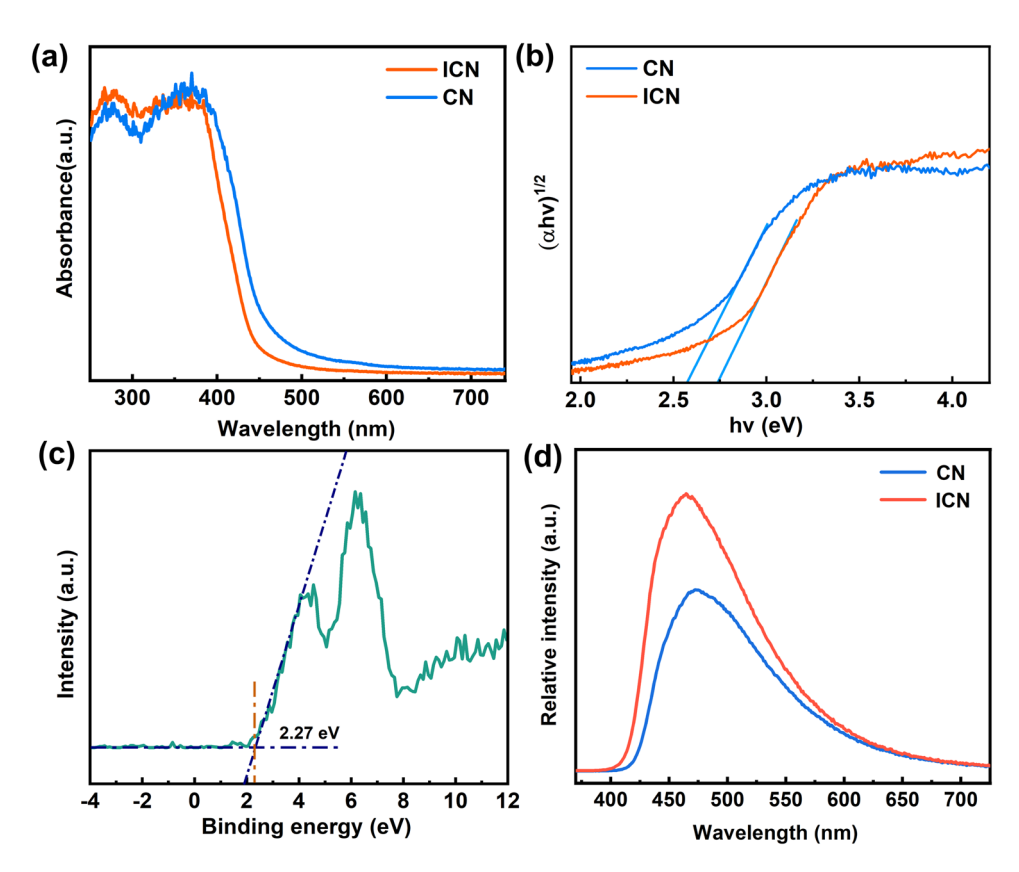


Figure 11: (a) UV-Vis reflectance spectra; (b) bandgap of CN and ICN; (c) XPS VB of ICN; (d) PL spectra of CN and ICN.

PL spectra can be used to evaluate the separation and recombination of photogenerated charges. Generally, a lower PL intensity indicates a more inhibited recombination of photogenerated electrons and holes, which is beneficial for photocatalytic activity. However, as shown in Figure 11d, the emission intensity of ICN is higher than that of CN, which is in agreement with the previous reports [35,36] explained by the reduction of particle size and the quantum confinement effect.

3.5 Photoelectrochemical properties

To further clarify the separation efficiency of photoexcited carriers, photocurrent response, EIS, and Mott–Schottky plots of CN and ICN were carried out. As demonstrated in Figure 12a, both CN and ICN display positive photocurrents by several on–off cycles. Noticeably, the photocurrent intensity of ICN is much stronger than that of CN, indicating a higher separation capacity of charge carriers, which is ascribed to the higher specific surface area. Figure 12b

shows the EIS Nyquist plots of CN and ICN. Generally, the smaller radius means a lower electron transfer resistance. It is clear that the radius of the ICN sample is smaller than that of CN both under light illumination and in the dark, which confirms that the ball milling process can enhance the charge transfer efficiency. In addition, the Mott–Schottky tests were also carried out. As shown in Figure 12c, a positive slope of CN and ICN can be observed, which confirms that the samples are n-type semiconductors. Besides, the charge carrier density ($N_{\rm D}$) can be estimated using the following formula [37]:

$$N_{\rm D} = \frac{2}{q\varepsilon\varepsilon_0} \frac{{\rm d}E}{{\rm d}(1/C^2)} = \frac{2}{q\varepsilon\varepsilon_0} \frac{1}{{\rm slope}},$$
 (4)

where q, ε , and ε_0 are the electron charge (1.6×10^{-19} C), the dielectric constant (5.25 for g- C_3N_4), and vacuum permittivity ($8.85 \times 10^{-14} \, \mathrm{F \cdot cm^{-1}}$), respectively. Hence, the charge carrier density of CN and ICN can be calculated as 3.85×10^{20} and $5.34 \times 10^{20} \, \mathrm{cm^{-3}}$, respectively. It is obvious that the carrier density of ICN is larger than that of pristine CN, inferring the higher electron concentration produced by ball milling.

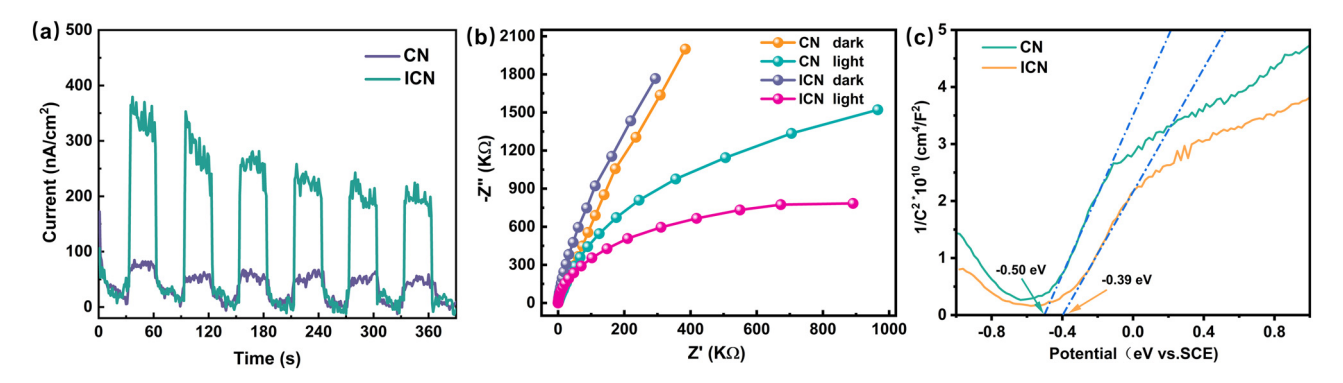


Figure 12: (a) Transient photocurrent response, (b) electrochemical impedance spectra, and (c) Mott-Schottky plots of CN and ICN.

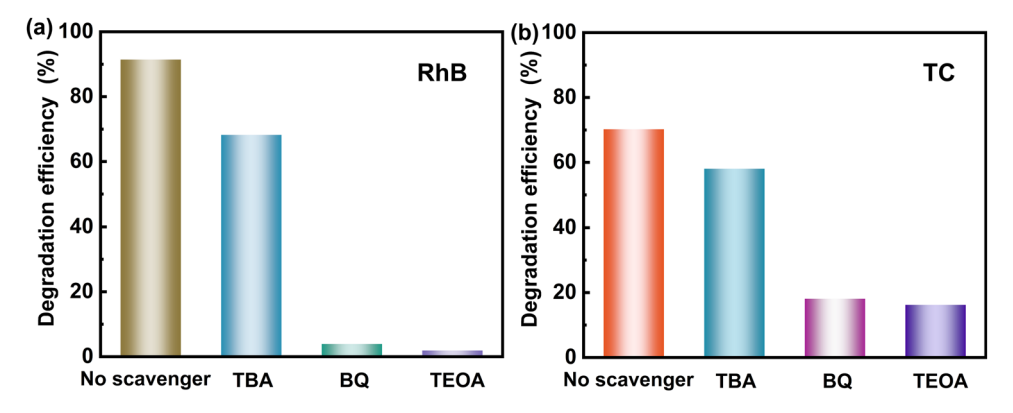


Figure 13: Effect of different quenchers on the degradation of (a) RhB and (b) TC over the ICN sample.

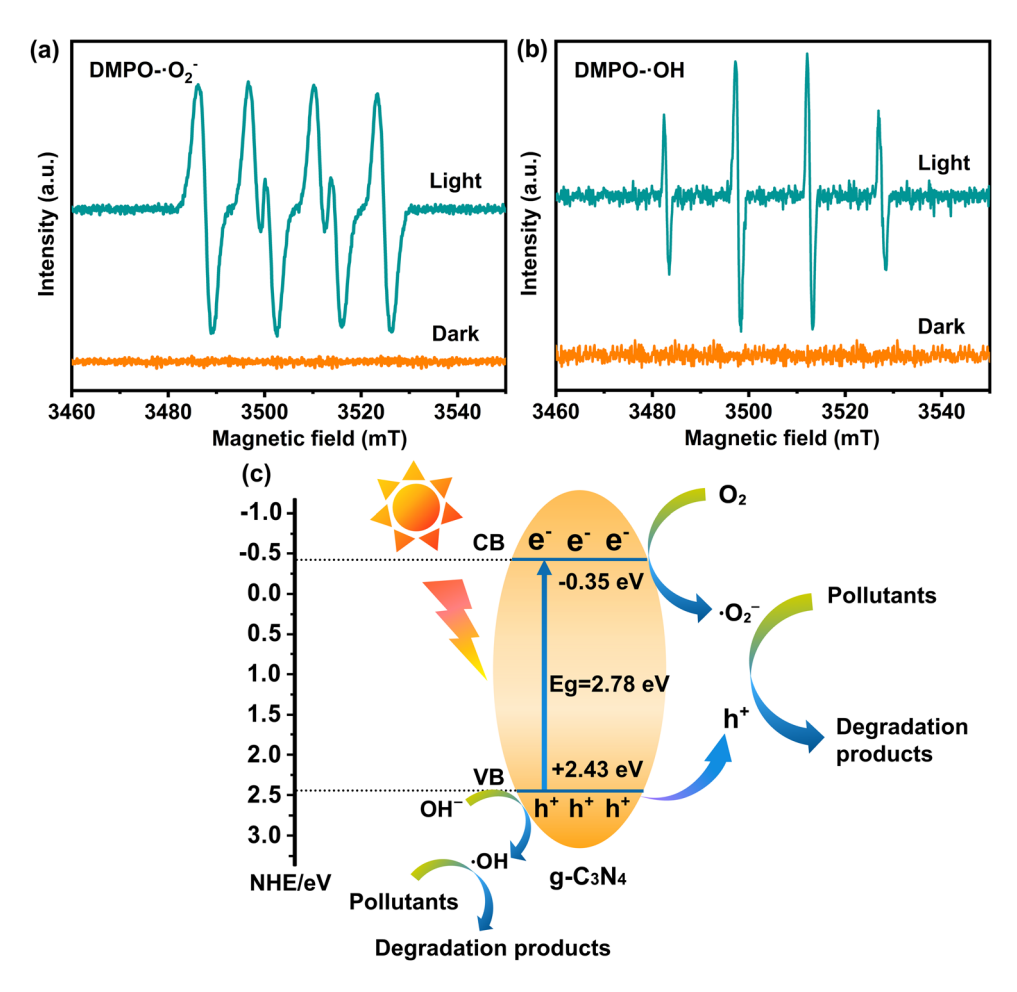


Figure 14: ESR spectra of (a) DMPO- $^{\circ}O_{2}^{-}$ and (b) DMPO- $^{\circ}OH$ for ICN under dark and light irradiation; (c) schematic of the photocatalytic reaction mechanism of organic pollutants.

3.6 Photocatalytic mechanism

To identify the main active species during the photocatalytic reaction, the trapping experiment was performed using various scavengers. TEOA (15 mM), TBA (10 mM), and BQ (1 mM) were used to capture holes (h $^+$), hydroxyl radicals (OH), and superoxide radicals (O $_2$ $^-$), respectively. Figure 13a shows that the degradation efficiency of RhB dramatically decreases to 68.2, 3.9, and 1.9% in the presence of TBA, BQ, and TEOA, respectively. Similarly, after the addition of TBA, BQ, and TEOA, the photodegradation efficiency of TC drops to 58.1, 18.1, and 16.2% (Figure 13b), respectively. It can be concluded that h $^+$ and $^+$ O $_2$ $^-$ are the main active species, whereas OH has a minor effect on the degradation reaction.

The generation of free radicals in the photocatalytic reactions can be detected by ESR using DMPO as the trapping agent. As demonstrated in Figure 14a, there is no characteristic peak of O_2^- in the dark. After light irradiation, four characteristic peaks of O_2^- with an intensity of

1:1:11 can apparently be observed. Similarly, four peaks with relative intensity of 1:2:2:1 corresponding to 'OH could be clearly seen in Figure 14b after 5 min of light irradiation, whereas no ESR signals appear in the dark. The ESR results further verify the presence of ' O_2^- and 'OH free radicals produced by ICN nanosheets, which is in accordance with the trapping experiment results.

Based on the above considerations, a possible photocatalysis mechanism for the ICN sample is proposed in Figure 14c. Under irradiation, the photogenerated electrons excited from ICN are transferred to the CB, leaving holes in the VB. The CB potential is more negative than the standard reduction potential of O_2/O_2^- (-0.33 V vs NHE), so the photogenerated electrons on the CB can react with O_2 to produce O_2^- , which has a strong oxidizing capacity and can directly participate in the oxidation of organic pollutants [38]. Meanwhile, the VB potential of ICN is more positive than the standard oxidation potential of OH/OH^- (+2.4 eV vs NHE), which means H_2O could be oxidized to OH by holes. Moreover, the photogenerated holes in the VB

of ICN can also directly oxidize pollutants. For RhB and TC degradation, the main active species (O_2^- and h^+) and assistant species (OH) produced on the surface of ICN could effectively degrade RhB and TC to CO2, H2O, and other small molecules [39]. In summary, the enhanced photocatalytic activity of g-C₃N₄ nanosheets is mainly attributed to the following factors: (1) the larger BET surface area, which can produce more electron-hole pairs and provide more active sites; (2) the faster charge carrier transfer rate, which improves the quantum efficiency.

4 Conclusion

g-C₃N₄ nanosheets with excellent photocatalytic activity were synthesized using the simple ball milling method. The influence of ball-milling parameters on the structure, morphology, optical properties, photoelectrochemical properties, and photocatalytic activity of g-C₃N₄ nanosheets was systematically analyzed. The obtained ICN sample showed higher degradation efficiency of RhB (91.4%) and TC (70.2%) than the CN sample, which was owing to its nanosheet structure that could shorten charge transfer distance to the surface and increase specific surface area, exposing more active sites. A set of optimum ball milling parameters was obtained as follows: ball-to-powder weight ratio of 10:1, milling speed of 420 rpm, milling time of 24 h, and the addition of 4 mL IPA. This study provides an alternative to traditional chemical exfoliation methods used for the preparation of thin nanosheets and yields insights into the development of advanced photocatalysts for the degradation of organic pollutants.

Acknowledgments: The authors are thankful for the financial support from the National Natural Science Foundation of China (No. 51702027) and the Science and Technology Planning Project of Longquanyi, Chengdu (No. LQXKJ-KJXM-2022-04). In addition, they thank the anonymous reviewers for their fruitful suggestions to improve the article.

Funding information: This research was supported by the National Natural Science Foundation of China (No. 51702027) and the Science and Technology Planning Project of Longquanyi, Chengdu (No. LQXKJ-KJXM-2022-04).

Author contributions: All authors have accepted responsibility for the entire content of this manuscript and approved its submission.

Conflict of interest: The authors state no conflict of interest.

Data availability statement: The datasets generated during and/or analysed during the current study are available from the corresponding author on reasonable request.

References

- Ibrahim, R. K., M. Hayyan, M. A. AlSaadi, A. Hayyan, and S. Ibrahim. Environmental application of nanotechnology: Air, soil, and water. Environmental Science and Pollution Research International, Vol. 239, 2016, pp. 13754-13788.
- Zhang, Y., J. Yuan, Y. Ding, B. Liu, L. Zhao, and S. Zhang. Research progress on $g\text{-}C_3N_4\text{-}based$ photocatalysts for organic pollutants degradation in wastewater: From exciton and carrier perspectives. Ceramics International, Vol. 47, 2021, pp. 31005-310030.
- Liu, X., R. Ma, L. Zhuang, B. Hu, J. Chen, X. Liu, et al. Recent developments of doped q-C₃N₄ photocatalysts for the degradation of organic pollutants. Critical Reviews in Environmental Science and Technology, Vol. 51, 2021, pp. 751-790.
- [4] Guan, Y., Z. Ren, Y. Lang, T. Liu, Z. Gong, and Y. Lv. Preparation and photocatalytic degradation of sulfamethoxazole by g-C₃N₄ nanocomposite samples. Reviews on Advanced Materials Science, Vol. 62, 2023, id. 20220280.
- [5] Inagaki, M., T. Tsumura, T. Kinumoto, and M. Toyoda. Graphitic carbon nitrides (g-C₃N₄) with comparative discussion to carbon materials. Carbon, Vol. 141, 2018, pp. 580-607.
- [6] Wang, F., J. Xu, Z. Wang, Y. Lou, C. Pan, and Y. Zhu. Unprecedentedly efficient mineralization performance of photocatalysis-self-Fenton system towards organic pollutants over oxygen-doped porous g-C₃N₄ nanosheets. Applied Catalysis B: Environmental, Vol. 312, 2022, id. 121438.
- Thomas, A., A. Fischer, F. Goettmann, M. Antonietti, J. O. Müller, R. Schlögl, et al. Graphitic carbon nitride materials: Variation of structure and morphology and their use as metal-free catalysts. Journal of Materials Chemistry, Vol. 18, 2008, pp. 4893-4908.
- Dong, F., L. Wu, Y. Sun, M. Fu, Z. Wu, and S. C. Lee. Efficient synthesis of polymeric g-C₃N₄ layered materials as novel efficient visible light driven photocatalysts. Journal of Materials Chemistry, Vol. 21, 2011, pp. 15171-15174.
- [9] Guo, Y., J. Li, Z. Gao, X. Zhu, Y. Liu, Z. Wei, et al. A simple and effective method for fabricating novel p-n heterojunction photocatalyst g-C₃N₄/Bi₄Ti₃O₁₂ and its photocatalytic performances. Applied Catalysis B: Environmental, Vol. 192, 2016, pp. 57-71.
- Lin, Y., G. V. C. Dizon, K. Yamada, C. Liu, A. Venault, H. Lin, et al. Sulfur-doped g-C₃N₄ nanosheets for photocatalysis: Z-scheme water splitting and decreased biofouling. Journal of Colloid and Interface Science, Vol. 567, 2020, pp. 202-212.
- [11] Wang, T., J. Zheng, J. Cai, Q. Liu, and X. Zhang. Visible-light-driven photocatalytic degradation of dye and antibiotics by activated biochar composited with K⁺ doped q-C₃N₄: Effects, mechanisms, actual wastewater treatment and disinfection. Science of the Total Environment, Vol. 839, 2022, id. 155955.
- Yang, C., F. Zhang, X. Liu, Y. Du, D. Huang, J. Liu, et al. Long afterglow phosphor driven g-C₃N₄ photocatalyst for continuous water purification under light and dark conditions. Journal of Solid State Chemistry, Vol. 310, 2022, id. 123057.
- Li, D., W. Huang, L. Zou, A. Pan, and G. Huang. Mesoporous g-C₃N₄ nanosheets, synthesis, superior adsorption capacity and

- photocatalytic activity. Journal of Nanoscience and Nanotechnology, Vol. 18, 2018, pp. 5502-5510.
- [14] Wu, X., J. Cheng, X. Li, Y. Li, and K. Lv. Enhanced visible photocatalytic oxidation of NO by repeated calcination of g-C₃N₄. Applied Surface Science, Vol. 465, 2019, pp. 1037-1046.
- [15] Zhang, X., X. Xie, H. Wang, J. Zhang, B. Pan, and Y. Xie. Enhanced photoresponsive ultrathin graphitic-phase C₃N₄ nanosheets for bioimaging. Journal of the American Chemical Society, Vol. 135, 2013,
- [16] Ma, Z., P. Zhou, L. Zhang, Y. Zhong, X. Sui, B. Wang, et al. g-C₃N₄ nanosheets exfoliated by green wet ball milling process for photodegradation of organic pollutants. Chemical Physics Letters, Vol. 766, 2021, id. 138335.
- [17] Zhu, K., Y. Lv, J. Liu, W. Wang, C. Wang, S. Li, et al. Facile fabrication of g-C₃N₄/SnO₂ composites and ball milling treatment for enhanced photocatalytic performance. Journal of Alloys and Compounds, Vol. 802, 2019, pp. 13-18.
- [18] Beyhagi, A., S. M. T. Azimi, Z. Chen, C. Hu, and Q. Zeng. Exfoliated and plicated q-C₃N₄ nanosheets for efficient photocatalytic organic degradation and hydrogen evolution. International Journal of Hydrogen Energy, Vol. 46, 2021, pp. 20547-20559.
- [19] Zhu, K., W. Wang, A. Meng, M. Zhao, J. Wang, M. Zhao, et al. Mechanically exfoliated g-C₃N₄ thin nanosheets by ball milling as high performance photocatalysts. RSC Advances, Vol. 5, 2015, pp. 56239-56243.
- [20] Wei, X., X. Wang, Y. Pu, A. Liu, C. Chen, W. Zou, et al. Facile ballmilling synthesis of CeO₂/g-C₃N₄ Z-scheme heterojunction for synergistic adsorption and photodegradation of methylene blue: Characteristics, kinetics, models, and mechanisms. Chemical Engineering Journal, Vol. 420, 2021, id. 127719.
- [21] Li, X., B. Kang, F. Dong, Z. Zhang, X. Luo, L. Han, et al. Enhanced photocatalytic degradation and H₂/H₂O₂ production performance of S-pCN/WO_{2.72} S-scheme heterojunction with appropriate surface oxygen vacancies. Nano Energy, Vol. 81, 2021, id. 105671.
- [22] Zhang, W., D. Xu, F. Wang, and M. Chen. AgCl/Au/g-C₃N₄ ternary composites: Efficient photocatalysts for degradation of anionic dyes. Journal of Alloys and Compounds, Vol. 868, 2021,
- [23] Zhu, Y., X. Zhong, X. Jia, Q. Sun, and J. Yao. Geometry-tunable sulfurdoped carbon nitride nanotubes with high crystallinity for visible light nitrogen fixation. Chemical Engineering Journal, Vol. 431, 2022, id. 133412.
- [24] Mei, X., S. Chen, G. Wang, W. Chen, W. Lu, B. Zhang, et al. Metalfree carboxyl modified g-C₃N₄ for enhancing photocatalytic degradation activity of organic pollutants through peroxymonosulfate activation in wastewater under solar radiation. Journal of Solid State Chemistry, Vol. 310, 2022, id. 123053.
- [25] Zhao, Q., S. Liu, S. Chen, B. Ren, Y. Zhang, X. Luo, et al. Facile ballmilling synthesis of WO₃/g-C₃N₄ heterojunction for photocatalytic degradation of Rhodamine B. Chemical Physics Letters, Vol. 805, 2022, id. 139908.
- [26] Zhu, X., Y. Wang, Y. Guo, J. Wan, Y. Yan, Y. Zhou, et al. Environmental-friendly synthesis of heterojunction photocatalysts g-C₃N₄/BiPO₄ with enhanced photocatalytic performance. Applied Surface Science, Vol. 544, 2021, id. 148872.

- [27] Enayati, M. H., Z. Sadeghian, M. Salehi, and A. Saidi. The effect of milling parameters on the synthesis of Ni₃Al intermetallic compound by mechanical alloying. Materials Science and Engineering: A-Struct, Vol. 375, 2004, pp. 809-811.
- [28] Wang, X. L., W. Q. Fang, S. Yang, P. Liu, H. Zhao, and H. G. Yang. Structure disorder of graphitic carbon nitride induced by liquidassisted grinding for enhanced photocatalytic conversion. RSC Advances, Vol. 4, 2014, pp. 10676-10679.
- [29] Yin, Z., Q. Zhang, S. Li, G. Cagnetta, J. Huang, S. Deng, et al. Mechanochemical synthesis of catalysts and reagents for water decontamination: Recent advances and perspective. Science of the Total Environment, Vol. 825, 2022, id. 153992.
- [30] Cai, Q., J. Shen, Y. Feng, Q. Shen, and H. Yang. Template-free preparation and characterization of nanoporous α-C₃N₄ with enhanced visible photocatalytic activity. Journal of Alloys and Compounds, Vol. 628, 2015, pp. 372-378.
- [31] Patil, A. G. and S. Anandhan. Influence of planetary ball milling parameters on the mechano-chemical activation of fly ash. Powder Technology, Vol. 281, 2015, pp. 151-158.
- [32] Zhang, Z., X. Chen, S. Chen, Q. Dong, X. Zhang, A. Jiang, et al. Synergistic interaction of Z-scheme TiO₂/g-C₃N₄ photocatalyst and peroxymonosulfate for improving the photocatalytic efficiency of Rhodamine B. Optical Materials (Amsterdam, Netherlands), Vol. 133, 2022, id. 113081.
- [33] Kim, J. S., J. W. Oh, and S. I. Woo. Investigation for the effects of ball milling process on the physical characteristics, the behaviors of carriers and the photocatalytic activity of sulfur doped q-C₃N₄. International Journal of Hydrogen Energy, Vol. 42, 2017, pp. 5485-5495.
- [34] Wang, T., J. Cai, J. Zheng, K. Fang, I. Hussain, and D. Z. Husein. Facile synthesis of activated biochar/BiVO₄ heterojunction photocatalyst to enhance visible light efficient degradation for dye and antibiotics: Applications and mechanisms. Journal of Materials Research and Technology, Vol. 19, 2022, pp. 5017-5036.
- [35] Kim, J. S., J. W. Oh, and S. I. Woo. Improvement of the photocatalytic hydrogen production rate of g-C₃N₄ following the elimination of defects on the surface. Catalysis Today, Vol. 293,
- [36] Dong, F., Z. Wang, Y. Sun, W. Ho, and H. Zhang. Engineering the nanoarchitecture and texture of polymeric carbon nitride semiconductor for enhanced visible light photocatalytic activity. Journal of Colloid and Interface Science, Vol. 401, 2013, pp. 70-79.
- [37] Yang, Y., C. Zhang, D. Huang, G. Zeng, J. Huang, C. Lai, et al. Boron nitride quantum dots decorated ultrathin porous g-C₃N₄: Intensified exciton dissociation and charge transfer for promoting visible-light-driven molecular oxygen activation. Applied Catalysis B: Environmental, Vol. 245, 2019, pp. 87-99.
- [38] Lian, X., Y. Li, Y. Zou, D. An, Q. Wang, Q. Zhou, et al. High vis-light photocatalytic property of g-C₃N₄ on four pollutants (RhB, MB, TC-HCl and P-Nitrophenol). Current Applied Physics, Vol. 39, 2022,
- [39] Liu, W., M. Sun, Z. Ding, Q. Zeng, Y. Zheng, W. Sun, et al. Ball milling synthesis of porous q-C₃N₄ ultrathin nanosheets functionalized with alkynyl groups for strengthened photocatalytic activity. Separation and Purification Technology, Vol. 282, 2022, id. 120097.